



**HAL**  
open science

## Electromagnetic pulse generator: An analytical and numerical study of the Lorentz force in tube crimping processes

Khadija Sofi, Mohammed Hamzaoui, Hassan El Idrissi, Ahmed Nait Sidi Moh, Denis Jouaffre, Abdelkrim Hamzaoui

► **To cite this version:**

Khadija Sofi, Mohammed Hamzaoui, Hassan El Idrissi, Ahmed Nait Sidi Moh, Denis Jouaffre, et al.. Electromagnetic pulse generator: An analytical and numerical study of the Lorentz force in tube crimping processes. CIRP Journal of Manufacturing Science and Technology, 2020, 31, pp.108 - 118. 10.1016/j.cirpj.2020.10.002 . hal-03493536

**HAL Id: hal-03493536**

**<https://hal.science/hal-03493536>**

Submitted on 21 Nov 2022

**HAL** is a multi-disciplinary open access archive for the deposit and dissemination of scientific research documents, whether they are published or not. The documents may come from teaching and research institutions in France or abroad, or from public or private research centers.

L'archive ouverte pluridisciplinaire **HAL**, est destinée au dépôt et à la diffusion de documents scientifiques de niveau recherche, publiés ou non, émanant des établissements d'enseignement et de recherche français ou étrangers, des laboratoires publics ou privés.



Distributed under a Creative Commons Attribution - NonCommercial 4.0 International License

# Electromagnetic pulse generator: an analytical and numerical study of the Lorentz force in tube crimping processes

Khadija SOFI<sup>a,b,\*</sup>, Mohammed HAMZAOU<sup>b</sup>, Hassan EL IDRISSE<sup>a</sup>, Ahmed NAIT SIDI MOH<sup>b</sup>, Denis JOUAFFRE<sup>c</sup>, Abdelkrim HAMZAOU<sup>d</sup>

<sup>a</sup>*LEEA-TI, Department of electrical engineering, FSTM, Hassan II University of Casablanca, Mohammedia, Morocco*

<sup>b</sup>*LTI, Intelligent Systems team, EDSTS 585, University of Picardie Jules Verne, Saint-Quentin, France*

<sup>c</sup>*PFT Innovaltech - Lycée Condorcet, Saint-Quentin, France*

<sup>d</sup>*LGECOS, Department of electrical engineering, Cadi Ayyad University, ENSA, Marrakesh, Morocco*

---

## Abstract

In this paper, we address the application of Lorentz force in the electromagnetic pulse crimping process. To do so, we used an analytical method based on mutual inductance and mutual force between two circular coils. This crimping process is employed on conductive materials considered as work-pieces. For different voltages, we developed an analytical model for two circular coils corresponding to the inductance of the coil attached to RLC circuit, and the tube inductance. The magnetic density into the work-piece, the Lorentz force and the magnetic pressure on the tube are evaluated. Obtained results from experimental measurements and simulation are promising.

*Keywords:* Magnetic pulse generator, single turn coil, dissimilar materials welding, electrical scheme, current pulse

---

## 1. Introduction

In the new technology of magnetic pulse joining metal work-pieces, estimating the exact mechanical or magnetic force is essential for a wide range

---

\*Corresponding author

Email address: [khadija.sofi@etud.u-picardie.fr](mailto:khadija.sofi@etud.u-picardie.fr) (Khadija SOFI)

of scientific and industrial processes. The magnetic pulse crimping process is  
5 a high-velocity crimping method of metallic tubes using a magnetic field generated by an EMPG (ElectroMagnetic Pulse Generator). In the field of metallurgy, the EMPG has been studied by many researchers using massive coils and field shapers. The field shaper is a metallic piece used to adapt the massive coil to the deformation area of the metal work-piece [1]. It generally leads  
10 to a concentration of the magnetic field that acts on work-pieces in a specific area. As demonstrated in many studies over the last two years, due to the eco-environmental benefits of the magnetic forming process, the development of this technology has great potential for industrial purposes. In terms of the generated magnetic field and negative effect on electronic components such as  
15 sensors, many previous studies brought into question the safety of the EMPG [2]. Some of the studies were focused on reducing the adverse effects of the magnetic field on human health [3]. On the other hand, in terms of the force generated by EMPG, many researchers have consistently focused on studying the Lorentz force applied to work-pieces using finite element methods.

20 The third important parameter concerning EMPG is the temperature. Indeed, the temperature distribution is studied experimentally during the forming process and the results are that with a current pulse with a peak of  $150\text{ kA}$ , the active area in the massive coil reaches a maximum temperature of  $34^\circ\text{C}$ . This process is called cold forming [4]. In the literature, there has been considerable  
25 work addressed to the magnetic force produced in the crimping process of a tube. These studies are performed analytically, for example, using a method of splitting the massive coil into areas that correspond to uniform current. The calculation process depends on magnetic vector potential [5]. Other research works are performed by numerical simulations using FEM (Finite Element Method)  
30 and BEM (Boundary Element Method). Many studies about EMPG have focused on identifying and evaluating semi-analytical methods using, either the vector potential  $A$  or the injected current and the total energy stored in the EMPG [5].

In the electromagnetic forming process, a new investigation gives us an in-

35 sight into the geometry of a pressure coil. It presents an analytical method  
 to determine the optimum geometry of the coil. This method is based on two  
 parameters, the produced magnetic pressure on the work-piece and the mag-  
 netic energy generated by the EMPG. In this paper, the expression "forming"  
 will designate all magnetic pulse deforming processes. The present research  
 40 work predominately focuses on the analysis of the crimping process of an alu-  
 minum tube. As illustrated in figure 1, high power bank capacitors are charged  
 throughout a transformer, then discharged in the massive coil instantaneously  
 throughout spark-gaps. The discharged current creates an intense magnetic field  
 throughout spark-gaps. The discharged current creates an intense magnetic field  
 in the forming area and generates an eddy current in the work-piece (tube). The  
 45 Lorentz force is generated radially in the active area due to the magnetic field  
 produced by the coil and acts mechanically on the work-piece, which leads to the  
 crimping process. This process is performed without physical contact between  
 the tube and the massive coil. The active area or the working zone defines the  
 gap between the coil and the work-piece.

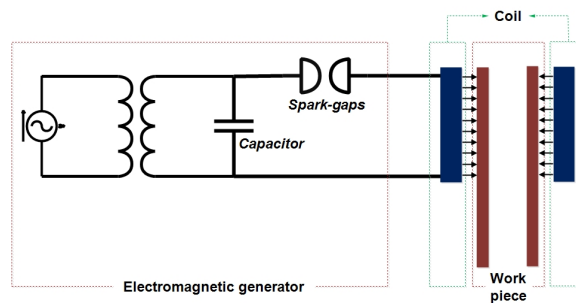


Figure 1: Electromagnetic pulse generator: tube crimping setup

50

Nowadays, several studies have also investigated electromagnetic welding  
 processes. In this research field, [6] explains the formation mechanism of two  
 kinds of wave interfaces in a Fe/Al electromagnetic welding process. Another  
 study [7] proposed a model to predict the critical wall thickness of the inner tube  
 55 in the same process. The thickness of the tube has been verified experimentally  
 with an error of less than 2.5%. A recent study of the same team of researchers

has investigated the magnetic pulse welding of tubular carbon-fiber-reinforced plastic / aluminum [8]. In an analysis of crimped connections realized by the same process, [9] gives an analytic model to predict the joining zone parameters that was verified experimentally. In a recent study, the magnetic pressure is predicted analytically, by numerical simulations and verified experimentally [10]. This study is very interesting as it takes into account all the work-pieces, the materials properties and the EMPG parameters used in the process. Authors of [11] stated in their research work the advantages of the electromagnetic crimping process over conventional ones. Authors established an Al to copper wire crimping process, the average gap in this case, was minimized by 70% and the pullout strength reaches  $1.958kN$  rather than  $0.98kN$  in the conventional method. As noted in a recent study [12], the trapezoidal shape of the coil increases the velocity of the wire's crimping by 10% compared to circular or rectangular coils. In order to find the right coil dimensions and the discharge voltage, the same authors conducted numerical simulation research about the copper wire crimping process [13]. The joint properties in the electromagnetic crimping process have also been studied earlier in [14] using metallic filler materials. Authors of the study proved that the filler materials increase the load-bearing capacity. The velocity in the electromagnetic joining process is also studied in the literature. An example of the joining of Al tube to steel rods have been established in [15], it shows that the velocity of the joining reaches a maximum value of  $500m/s$ . The same research team studied the velocity in the joining of steel to steel tubes [16]. In this case, the speed reaches  $360m/s$ .

To the best of our knowledge today, very little research has been done on the exact Lorentz force needed for the whole process. Most of this research has been performed experimentally [17] or by numerical simulations using FEM [18]. For the analytical studies, the method has been based on the calculation of the inductance of both the primary coil and the work-piece to determine magnetic pressure is performed in the following studies [19, 20]. A significant part of our research in this paper is focused on the calculation of self and mutual inductance of both the coil and the work-piece. This leads us to determine analytically the

radial Lorentz force needed to achieve the desired deformation. Thus, using the stress/strain modeling of the material of a work-piece, specifically a model that involves a high strain rate deformation of metallic parts, we can predict the velocity of the deformation, the displacement and finally the final shape of this work-piece. This part of the study is not concluded in the paper However, it is considered as part of future research work. Previous research worked on defining self and mutual inductance of complicated geometries using three dimensional configurations which are presented in [21, 22]. Another critical study has been developed in [23] using Bessel functions to calculate the inductance of non-coaxial coils. Regarding the Lorentz force, the authors of [24] identify a three dimensional analytical case where they have investigated the mutual Lorentz force of two thick coils using Biot & Savart's law. This study found that the force decreases when the distance between the two coils increases, while the maximum force is reached when the distance is the minimum possible. Since there is no contact between the coil and the tube, we consider this process as an energy transfer system. In the same vein, a thesis based on the same principle presented a wireless energy transfer in a system which rotates on two axes using air transformers [25]. In this thesis both mutual inductance of coaxial and non-coaxial rectangular or circular coils are investigated. In the same field of electromagnetic forming, a case study is based on 1D analytical modelling of the coil and determines the electro-mechanical parameters by defining the magnetic vector potential [5]. Together these studies provide valuable insights into the electromagnetic crimping process and the parameters needed to be defined before using experimental setup applications. Compared with studies that have been already developed in the literature, the main advantage of our study is that the analytical method is based only on the geometry of the coil to measure the current in the coil and other electro-mechanical parameters of the electromagnetic crimping process. There are several important areas where this study can make an original contribution to the electromagnetic forming processes. A specific objective of this study is to predict preliminary the voltage load and the geometry of the work-piece before performing experimental measurement

and starting to produce the final product industrially. It can also predict the  
120 velocity of the crimping process, which will help to automate the process.

The remainder of this paper is as follows: Analytical modelling theory is given  
in section 2, where we calculate the mutual inductance between the coil and the  
tube. In addition, we compute the magnetic field generated in the working zone  
and the Lorentz force applied on the tube. Section 3 presents the numerical  
125 method using FEM and BEM. This method predicts the magnetic pressure re-  
quired to produce the final shape of the work-piece after the crimping process.  
Numerical simulations are performed using coupled mechanical, thermal and  
electromagnetic solvers in LS-DYNA software [26, 27]. Results of both studies  
are detailed in section 5, where we focus mainly on comparing Lorentz force  
130 both analytically and numerically. Section 6 is the conclusion and gives some  
perspectives and future directions for this work.

## 2. System analytical modelling

In the electromagnetic pulse generator, the interaction between the coil and  
work-pieces is performed by the mutual inductance and mutual Lorentz force.  
135 Furthermore, the eddy current generated in the tube is based on the magnetic  
field generated itself by the coil. The Lorentz force acting on the tube is due to  
both the magnetic field produced by the coil and the eddy current in the tube.  
Using the electrical scheme of the EMPG represented in figure 2, we develop an  
analytical model based on the Neumann formula of mutual inductance between  
140 two circular coils. This model will be used to specify the Lorentz force and its  
impact on the tube deformation. This method enables the calculation of the  
self and mutual inductance using only the geometry of the main coil, and it de-  
termines the current using these parameters. The calculation method expresses  
precisely the Lorentz force needed for a specific deformation of the work-piece.  
145 To establish the current pulse shape in the coil, we begin by giving an overall  
equation of the current based on an RLC circuit study using an experimental  
measurement of these parameters. Then, we develop an analytical method for

the mutual inductance and self-inductance inside the massive coil. The purpose here is to give the exact current shape using only the coil geometry. This result will allow us to express the magnetic field and Lorentz force analytically in a short period of time compared to numerical analysis.

### 2.1. Electrical scheme of the EMPG

The main electrical scheme that explains the circuit of the process is illustrated in figure 2. The capacitor  $C_1$  represents the bank capacitors. The coil is expressed by an  $RL$  series circuit ( $R$  is the resistance of the coil, and  $L$  is its inductance) conducts a current  $I_c$ , while the tube, conducts the current  $I_t$ , is expressed by an  $RL$  series circuit ( $L_t$  is the inductance of the tube and  $R_t$  is its resistance). The current is conducted by coaxial cables (24 cables) which connect the bank of capacitors to the main coil. The electrical scheme of these conductors is also an  $RLC$  circuit, presented by  $C_2$ ,  $R_c$  and  $L_c$  and represent, respectively, the capacity, the resistance, and the inductance of the cables. In figure 2, we represent the total inductance and resistance of the primary circuit, which are  $L_p = L_c + L$  and  $R_p = R_c + R$ . The resistance, self and mutual inductance of the scheme is calculated in the next section. In figure 2, the

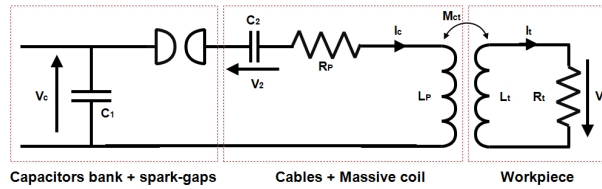


Figure 2: Electrical scheme of the EMPG

coil and the tube acts as an air transformer, which is governed by Eq. (1). The voltage  $V_c$  is defined using the mutual inductance  $M_{ct}$  between the coil and the tube.  $V_c$  and  $V_t$  are respectively, the voltages in the capacitor  $C_1$  and in the tube. Using Laplace transfer, we get the resulting expressions in Eq. (1).

$$\begin{cases} V_c(p) = V_2(p) + R_p I_c(p) + pL_p I_c(p) + pM_{ct} I_t(p) \\ V_t(p) = R_t I_t(p) + pL_t I_t(p) + pM_{ct} I_c(p) = 0 \end{cases} \quad (1)$$

From  $V_2(p)$  and  $V_t(p)$  expressed in Eq. (1), we get the following expressions for currents  $I_c$  and  $I_t$ .

$$\begin{cases} I_t(p) = -\frac{pM_{ct}}{R_t + pL_t}I_c(p) \\ I_c(p) = -p C_1V_c(p) = p C_2V_2(p) \end{cases} \quad (2)$$

During the procedure that we followed, the parasitic capacitance in the coil is considered very small and does not have a significant effect on the current pulse. Therefore, we ignore the parasitic capacitance during the calculation of the current.  $I_c$  symbolizes the current pulse flowing through the coil, and  $I_t$  is the current generated in the tube.

From Eq. (1) and Eq. (2), we obtain the differential equation (3). It expresses the electrical behavior of the EMPG.

$$\begin{aligned} R_t(1 + \frac{C_1}{C_2})v_c(t) + (L_t(1 + \frac{C_1}{C_2}) + R_pR_tC_1)\frac{dv_c(t)}{dt} + \\ (R_pL_t + L_pR_t)C_1\frac{d^2v_c(t)}{dt^2} + (L_tL_p - M_{ct}^2)C_1\frac{d^3v_c(t)}{dt^3} = 0 \end{aligned} \quad (3)$$

In what follows, we begin the numerical simulation by injecting the computed current pulse into the coil in order to deform the tube. It is worth nothing that in the analytical section, the current settings calculated in the numerical analysis do not serve for the results. Only the peak of the current is computed using the self and the mutual inductance and depending only on the coil dimensions and the input voltage.

## 2.2. Self and Mutual Inductance

Mutual inductance is considered as one of the most useful parameters in numerous applications such as generators and transformers [28]. Therefore, since we have noticed an air core transformer system in our EMPG system, we have developed the following method; by identifying the mutual inductance between the coil and the tube. The massive coil and the tube's geometry are illustrated in figure 3. It is important to clarify that the geometric structure of the pieces is based on the experimental research in our previous studies [3, 4]. The current in the massive coil and the field shaper, represented in these studies,

circulates only in on the interior surface of the tube. Consequently, this massive coil can be replaced by a one-turn coil, as illustrated in figure 3.  $R_1$  and  $R_2$  represents the inner and outer radius of the coil respectively while  $R_3$  and  $R_4$  are respectively the inner and outer radius of the tube. The current is injected into two bars located at the gap of the coil represented by C in figure 3. To begin this

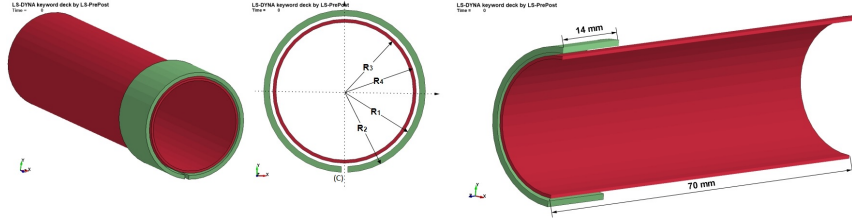


Figure 3: Geometric representation of the coil and the tube

process, we represent the coil or the tube in figure 4. First, we consider a hollow cylinder with  $R_{i1}$  as an inner radius and  $R_{i2}$  as an outer radius while its length is  $Z_{i2} - Z_{i1}$ . The cylinder generates a resistance  $R_{s_i}$  and a self-inductance  $L_i$ . Before computing the mutual inductance, we begin by using the expression of the self-inductance  $L_i$ . The method adopted in the calculation of the self-inductance

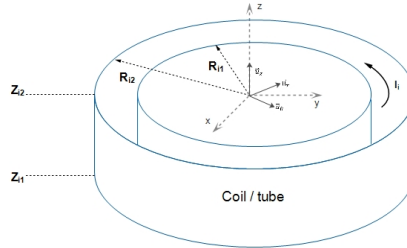


Figure 4: Representation of a hollow cylinder

$L_i$  has been developed in [29] for a rectangular coil, and expressed with the Cartesian coordinates  $x, y, z$  using a sextuplet definite integral. However, since we are using a cylinder coil in our study, the calculus will be developed with cylindrical coordinates. Therefore we give the following expression of  $L_i$  as

presented in Eq. (4).

$$L_i = \frac{\mu_0}{4\pi S_i^2} Q_i \quad (4)$$

where  $S_i^2 = (R_{i2} - R_{i1})^2 (Z_{i2} - Z_{i1})^2$  is the rectangular cross section surface.

$Q_i$  is expressed using the following definite integrals as shown in Eq. (5).

$$Q_i = \int_{\alpha}^{2\pi-\alpha} \int_{Z_{i1}}^{Z_{i2}} \int_{Z_{i1}}^{Z_{i2}} \int_{R_{i1}}^{R_{i2}} \int_{R_{i1}}^{R_{i2}} \frac{rR \cos(\theta) dR dr dZ dz d\theta}{\sqrt{r^2 + R^2 - 2rR \cos(\theta) + (z - Z)^2}} \quad (5)$$

In the analysis method, the integral of  $Q_i$  on  $\theta$  is performed between  $\alpha$  and  $2\pi - \alpha$ . Since the coil has a gap (C) for current input and output,  $\alpha \neq 0$  represents the angle at the beginning of the coil at the gap while in this case we perform the inductance of the tube with  $\alpha = 0$ . As a result, the primitive of  $Q_i$  is given in Eq. (6), and its integral is expressed by Eq. (7).

$$\begin{aligned} Q_i = & Q_i[r(2), t(2), z(2)] - Q_i[r(1), t(2), z(2)] - (Q_i[r(2), t(1), z(2)] - Q_i[r(1), t(1), z(2)]) \\ & - (Q_i[r(2), t(2), z(1)] - Q_i[r(1), t(2), z(1)]) - (Q_i[r(2), t(1), z(1)] - Q_i[r(1), t(1), z(1)]) \end{aligned} \quad (6)$$

where,  $r(1) = R_{i1}$ ,  $r(2) = R_{i2}$ ,  $\theta(1) = \alpha$ ,  $\theta(2) = 2\pi - \alpha$ ,  $z(1) = Z_{i1}$  and  $z(2) = Z_{i2}$ .

$$\begin{aligned} Q_i = & \frac{1}{72} \left[ \frac{6}{5} \left( r^4 \left( 1 - \frac{\sin^2(2\theta)}{2} - 3 \cos^2(\theta) \sin^2(\theta) \right) + z^2(z^2 - 3r^2) \right) \sqrt{r^2 + z^2} \right. \\ & - 12r^4 z \sin(\theta) \cos(\theta) z^2 \arctan \left( \frac{\sin(\theta) \cos(\theta)}{z \sqrt{r^2 + z^2}} \right) \\ & + \sin^2(\theta) \arctan \left( \frac{\cos(\theta) z}{\sin(\theta) \sqrt{r^2 + z^2}} \right) + \cos^2(\theta) \arctan \left( \frac{\sin(\theta) z}{\cos(\theta) \sqrt{r^2 + z^2}} \right) \\ & - 3r \cos(\theta) (r^2 \sin^2(\theta) (r^2 \sin^2(\theta) - 6z + z^4)) \ln(r \cos(\theta) + \sqrt{r^2 + z^2}) \\ & - 3r \sin(\theta) (r^2 \cos^2(\theta) (r^2 \cos^2(\theta) - 6z + z^4)) \ln(r \sin(\theta) + \sqrt{r^2 + z^2}) \\ & \left. - 3zr^4 \left( 1 - \frac{\sin^2(2\theta)}{2} - 6 \cos^2(\theta) \sin^2(\theta) \right) \ln(z + \sqrt{r^2 + z^2}) \right] \quad (7) \end{aligned}$$

In the second step we calculate the resistance  $Rs_i$ . To do so,  $Rs_i$  of each piece is calculated using the following expression  $Rs_i = \rho \cdot \frac{l}{S}$ , where  $l$  represents the length of the wire of each conductor,  $S$  is the cross-section area, and  $\rho$  represents

the electrical resistivity of the material. Based on this formula, the resistance is expressed by Eq. (8).

$$Rs_i = \rho \cdot \frac{\pi(R_2 + R_1)}{(R_2 - R_1)(Z_2 - Z_1)} \quad (8)$$

165 After calculating the resistance, the next step is the calculation of the mutual inductance  $M_{ct}$  between two coaxial hollow cylinder coils represented by the tube and the coil using Neumann formula. Figure 5 shows a 3D configuration of the coil in situ with the tube. The blue hollow cylinder (external piece) represents the coil of length  $Z_2 - Z_1$  while the red one (internal piece) represents the tube of length  $Z_4 - Z_3$ .

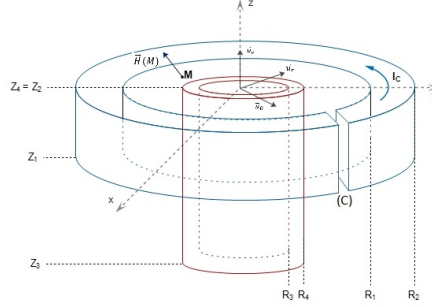


Figure 5: 3D Representation of the tube and the coil

170

According to a study developed by [28], the mutual inductance  $M_{ct}$  is given by Eq. (9). The parameter  $Q$  is expressed using integrals along  $r$ ,  $R$ ,  $z$ ,  $Z$  and  $\theta$  as given in Eq. (10).

$$M_{ct} = \frac{\mu_0}{(R_2 - R_1)^2 (Z_2 - Z_1)^2 (R_4 - R_3)^2 (Z_4 - Z_3)^2} Q \quad (9)$$

$$Q = \int_0^\pi \int_{Z_1}^{Z_2} \int_{Z_3}^{Z_4} \int_{R_1}^{R_2} \int_{R_3}^{R_4} \frac{rR \cos(\theta) dR dr dZ dz d\theta}{\sqrt{r^2 + R^2 - 2rR \cos(\theta) + (z - Z)^2}} \quad (10)$$

After integrating along  $r$ ,  $R$ ,  $z$  and  $Z$ , the expression of  $Q$  becomes:

$$Q = \int_0^\pi G[R_1, R_2, R_3, R_4, Z_1, Z_2, Z_3, Z_4, \theta] \cos(\theta) d\theta \quad (11)$$

where

$$G = [ [ [ [ F(r, R, z, Z, \theta) ]_{R_1}^{R_2} ]_{R_3}^{R_4} ]_{Z_1}^{Z_2} ]_{Z_3}^{Z_4} \quad (12)$$

Since  $F(r, R, z, Z, \theta) \cos(\theta)$  presents singularities at  $\theta = 0$  and  $\pi$ , the integral along  $\theta$  is solved using Newton cotes method of 1<sup>st</sup> order (Trapezoidal Rule) and L'Hospital's rule as expressed in Eq. (13) and in Eq. (14).

$$\int_a^b F(r, R, z, Z, \theta) \cos(\theta) d\theta = \frac{b-a}{2} [ F(r, R, z, Z, a) \cos(a) + F(r, R, z, Z, b) \cos(b) ] \quad (13)$$

$$\left\{ \begin{array}{l} \lim_{\theta \rightarrow 0} F(r, R, z, Z, \theta) \cos(\theta) = \frac{(z-Z)(r^2-R^2)^2}{8} \ln[z-Z+Y] + \frac{(z-Z)^2}{6} r^3 \ln[r-R+Y] + \\ \frac{(z-Z)^2}{6} R^3 \ln[R-r+Y] - \frac{(r-R)^2}{30} (r^2+3rR+R^2)Y - \\ \frac{Y(z-Z)^2}{20} \left( \frac{Y^2}{9} + \frac{rR}{3} + \frac{3(r^2+R^2)}{2} \right) \\ \lim_{\theta \rightarrow \pi} F(r, R, z, Z, \theta) \cos(\theta) = - \frac{(z-Z)(r^2-R^2)^2}{8} \ln[z-Z+X] \\ - \frac{(z-Z)^2}{6} (r^3+R^3) \ln[r+R+X] \\ + \frac{(r+R)^2}{30} (r^2-3rR+R^2)X + \\ \frac{X(z-Z)^2}{20} \left( \frac{X^2}{9} - \frac{rR}{3} + \frac{3(r^2+R^2)}{2} \right) \end{array} \right. \quad (14)$$

where:  $X = \sqrt{(r+R)^2 + (z-Z)^2}$  and  $Y = \sqrt{(r-R)^2 + (z-Z)^2}$ .

175 Based on the resistance, self-inductance and mutual inductance equations of the coil and the tube, we calculate the current in the next section. In addition, we define the magnetic field, Lorentz force and magnetic pressure, operating on the tube during the crimping process.

### 2.3. Governing equations of magnetic parameters

Dynamic deformation of metal pieces during welding or crimping is due to the magnetic loading condition. This deformation is obtained from the magnetic pressure which is, itself, generated by the Lorentz force [30]. To predict the required Lorentz force for the tube's crimping, we used a theoretical approach based on mutual forces and Biot & Savart's law in the working zone and the

current in the coil [31].

The current in the coil is calculated as stated in Eq. (2). From this equation, we extract the magnetic field strength using Biot & Savart's law at the point  $M(r, z)$  referring to figure 5. The magnetic field is expressed in Eq. (15). This allow us to establish the expression of the magnetic field at a point  $M(r, z)$  in the working zone. This means that the red tube represented in figure 5 is not taken into account while calculating the magnetic field.

The current density  $J$  flowing through the coil is expressed by:  $J = \frac{I_c}{(Z_2 - Z_1)(R_2 - R_1)}$ , and the magnetic field is expressed by:

$$\vec{H}(M) = \frac{1}{4\pi} \int \int \int_V \vec{J} d\vec{v} \wedge (-\nabla G(\vec{r}|\vec{r}')) \quad (15)$$

$G$  represents the Green's function in 3 dimensions. Supposing a point  $M(\tilde{r}, \tilde{z}, \tilde{\theta})$  that belongs to the coil,  $G$  will be given by the following equation:

$$G(\vec{r}|\vec{r}') = \frac{1}{|\vec{r} - \vec{r}'|} = \frac{1}{\sqrt{r^2 + \tilde{r}^2 - 2r\tilde{r}\cos(\tilde{\theta}) + (z - \tilde{z})^2}}$$

Therefore, the gradient of  $G$  is expressed as follows:  $-\nabla G(\vec{r}|\vec{r}') = \frac{\vec{r} - \vec{r}'}{|\vec{r} - \vec{r}'|^3}$

The radial and axial components of the magnetic field, represented respectively by  $H_r$  and  $H_z$  are expressed in Eq. (16).

$$\begin{cases} H_r(r, z) = \frac{J}{4\pi} \int_{R_1}^{R_2} \int_{\alpha}^{2\pi-\alpha} \int_{Z_1}^{Z_2} \frac{(z - \tilde{z}) \cos(\tilde{\theta}) \tilde{r} d\tilde{r} d\tilde{\theta} d\tilde{z}}{(r^2 + \tilde{r}^2 - 2r\tilde{r}\cos(\tilde{\theta}) + (z - \tilde{z})^2)^{3/2}} \\ H_z(r, z) = \frac{J}{4\pi} \int_{R_1}^{R_2} \int_{\alpha}^{2\pi-\alpha} \int_{Z_1}^{Z_2} \frac{(\tilde{r}) - r \cos(\tilde{\theta}) \tilde{r} d\tilde{r} d\tilde{\theta} d\tilde{z}}{(r^2 + \tilde{r}^2 - 2r\tilde{r}\cos(\tilde{\theta}) + (z - \tilde{z})^2)^{3/2}} \end{cases} \quad (16)$$

After integrating along  $\tilde{r}$  and  $\tilde{z}$ , final expressions of  $H_r$  and  $H_z$  are given in Eq. (17). The integral along  $\theta$  is done such as  $\alpha < \theta < 2\pi - \alpha$ .

$$\begin{cases} H_r(r, z) = \frac{J}{4\pi} \sum_{i,k=1}^2 (-1)^{i+k} \left\{ \phi((a+b)K(k) - aE(k)) + \int_{\alpha}^{2\pi-\alpha} \Psi_r d\theta \right\} \\ H_z(r, z) = \frac{J}{4\pi} \sum_{i,k=1}^2 (-1)^{i+k} \left\{ \int_{\alpha}^{2\pi-\alpha} (\Psi_z + f \ln[d+c]) d\theta \right\} \end{cases} \quad (17)$$

with:

$$\begin{cases} \Psi_r = r \cos^2(\theta) \ln[d + c] \\ \Psi_z = r \cos(\theta) \ln[f + c] + v \arctan\left(\frac{df \csc(\theta)}{rc}\right) - z_j + v \arctan\left(\frac{v}{f}\right) \end{cases} \quad (18)$$

Other parameters are defined as follows in table 1.

Table 1: Electrical parameters

$a$	$b$	$c$	$d$	$f$	$k$	$v$	$\phi$
$r^2 + r_i^2 + (z - z_k)^2$	$2rr_i$	$\sqrt{a - b \cos(\theta)}$	$r_i - r \cos(\theta)$	$z - z_k$	$r \sin(\theta)$	$r \sin(\theta)$	$\frac{4}{3} \frac{\sqrt{a-b}}{b}$

180

The expressions of elliptical integrals  $K(k)$  and  $E(k)$  are given in Eq. (19).

$$\begin{cases} K(k) = \int_0^{\pi/2} \frac{1}{\sqrt{1 - k \sin^2(\theta)}} d\theta \\ E(k) = \int_0^{\pi/2} \sqrt{1 - k \sin^2(\theta)} d\theta \end{cases} \quad (19)$$

The known formula of the magnetic induction  $\vec{B}$  is expressed in the general following Eq. (20).

$$\vec{B} = \mu \vec{H} \quad (20)$$

where:  $\vec{H} = H_r \cdot \vec{u}_r + H_z \cdot \vec{u}_z$

In the work-piece, the current density  $J_t$  is a function of  $B$  in Eq. (21). The parameter  $r$  represents the variable radius inside the tube. For simplification purposes, we suppose that the current density is uniform at each circle of radius  $r$  inside the tube.

$$\vec{J}_t = -\frac{\partial \vec{B}}{\mu \partial r} \quad (21)$$

where  $\mu$  represents the magnetic permeability of the material of the tube. The radial Lorentz force acting on the work-piece is given by the Eq. (22).

$$\vec{F} = \vec{J}_t \times \vec{B} \quad (22)$$

To simplify Lorentz force expression, we try to reduce the size of the magnetic field vector model as much as possible. In order to minimize the computational resources and time needed to resolve the model, we use symmetry and boundary

conditions of the model. After performing the numerical simulation, we found that the radial magnetic field  $H_r \simeq 0$ . Since the magnetic field vector  $\vec{B}$  has only the axial component  $B_z$  and  $\vec{J}_t$  is perpendicular to  $\vec{B}$ , the Lorentz force may be presented by Eq. (23) [19].

$$\vec{F} = -\frac{1}{\mu} \vec{B} \frac{\partial \vec{B}}{\partial r} = -\frac{1}{2\mu} \frac{\partial(\vec{B}^2)}{\partial r}. \quad (23)$$

The final step in the analytical method focuses on the expression of the magnetic pressure applied to the tube. Since in Eq. (23) we compute the volume magnetic force, then the magnetic pressure will be presented by the integral of this force along with the thickness of the tube as given in Eq. (24).

$$P = \int_0^d \vec{F} dy \quad (24)$$

where  $d$  represents the tube's thickness.

In the following section, we address a numerical method using FEM and BEM approaches and based on the presented geometry of figure 3.

### 3. Numerical method

After representing the system with the analytical method, a numerical method based on finite element method is performed to verify the analytical results of Lorentz force and magnetic field magnitudes. To do so, we first study the electromagnetic field based on Maxwell equations and the electromagnetic solver developed by LS-DYNA. From Maxwell equations, the current density is given in Eq. (25) and the magnetic field is expressed in Eq. (26).

$$\vec{J} = \sigma \vec{E} + \vec{J}_s \quad (25)$$

$$\vec{B} = \mu_0 \vec{H} = \vec{\nabla} \times \vec{A} \quad (26)$$

where  $\vec{A}$  is the magnetic vector potential. From Ampère's law, we obtain the electrical field  $\vec{E}$  as expressed in Eq. 27, where  $\phi$  is the electrical scalar potential.

$$\vec{E} = -\vec{\nabla} \phi - \frac{\partial \vec{A}}{\partial t} \quad (27)$$

As we use Coulomb gauge:  $\nabla(\sigma\vec{A}) = 0$  and since there is no charge accumulation, the charge density is  $\rho = 0$ . The parameter  $\sigma$  represents the electrical conductivity of the conductor. As a result, the scalar potential verifies the equations (28) and (29).

$$\nabla(\sigma\vec{\nabla}\phi) = 0 \quad (28)$$

$$\sigma\frac{\partial\vec{A}}{\partial t} + \vec{\nabla} \times \left(\frac{1}{\mu_0}\vec{\nabla} \times \vec{A}\right) + \sigma\vec{\nabla}\phi = \vec{J}_s \quad (29)$$

185 In this method, the expressions of the Lorentz force and the magnetic pressure are calculated using the same equations (23) and (24) used in the analytical method.

## 4. Numerical values of system parameters

### 4.1. Parameters of the EMPG

190 To address the current shape, it is crucial to state the EMPG parameters that are given experimentally by the manufacturer of the EMPG as shown in table 2. These parameters are taken into account in Eq. (3) to get the input voltage and the current across the coil, as stated in figure 6. In this figure, the current pulse corresponds to various voltage loads ( 2.5 kV, 5.5 kV, 8.5 kV).  
 195 The voltage 8.5 kV corresponds to the maximum load generated by the EMPG.

Table 2: EMPG parameters

$C_1$	$L_c$	$R_c$	$C_2$	Maximum Energy
690 $\mu F$	44 nH	2.4 m $\Omega$	2.112 nF	25 kJ

The current presented in figure 6 is obtained from experimental measurements through the coil during the process. It is measured using a Rogowski coil with a wide bandwidth (100 Hz to 5 MHz). The cutoff frequency has a value of 5 MHz. For each output voltage unit measured, the Rogowski coil  
 200 has a conversion value of 128kA/V and its sensitivity is 7mV/A. This current

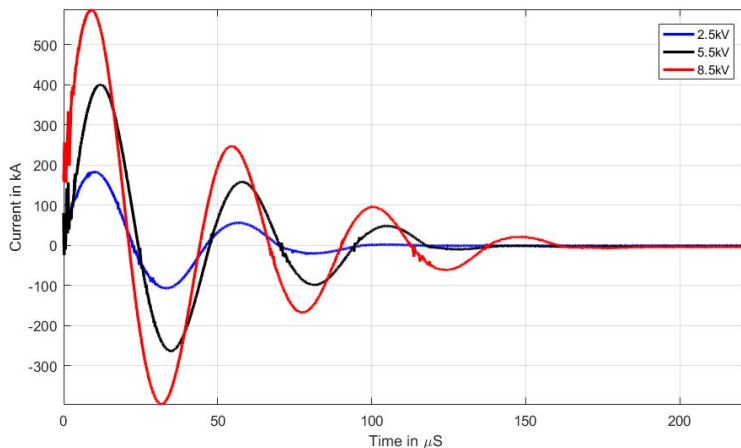


Figure 6: Current pulse variation in the massive coil

wave is loaded directly by using two bars inserted in the 3D model of the coil of the numerical simulations. The frequency  $f$  of the current pulse produced by 8.5 kV load is  $f = 20 \text{ kHz}$  as shown in figure 6 and the current peak is about  
 205 580 kA. At 5.5 kV, the current peak is 400 kA and at 2.5 kV, we reach 190 kA.

#### 4.2. 3D Modeling parameters

Material parameters used in analytical, simulation and experimental methods are given in table 3. In the finite element analysis approach, the Lorentz force is used as a load on the tubes to model their deformation in 3D. During  
 210 the process, we used a coil made of a copper alloy called siclanic® and a tube made of aluminium. Aluminum and siclanic® parameters have been addressed in [32].

As for the finite element analysis, the meshing of the coil and the tube is made only of hexahedron elements. The coil is decomposed to 3200 elements while  
 215 the tube has 8000 elements. In order to minimize the simulation's duration, we used BEM approach to mesh the air in the system. The boundary conditions are defined only in the elements close to the gap (C) presented in figure 3. These elements are used as the input and output bars of the currents injected the coil.

Table 3: Materials parameters

Parameters \ Materials	Siclanic ®	Aluminum
Mass density ( $kg/m^3$ )	8900	2700
Electrical resistivity ( $\Omega.cm$ )	$3.95e^{-6}$	$2.29e^{-6}$
Electrical conductivity ( $S/m$ )	$5.8e^7$	$3e^7$
Young's modulus ( $GPa$ )	130	68.9
Poisson's ratio	0.29	0.33

## 5. Obtained results

220 In this section, we report our obtained results during the analytical and the numerical simulation phases and give the most significant parameters and variables that impact the tube crimping process. It should be noted that the study of the impact of the tube's thickness is not addressed in this paper.

### 5.1. Numerical simulation results

225 The first set of analyses examine the impact of the voltage load on the tube's deformation and crimping at the current peak. In this section, The results are established using the following geometry configuration:  $R_1 = 11\text{ mm}$ ,  $R_2 = 11.5\text{ mm}$ ,  $R_3 = 10\text{ mm}$  and  $R_4 = 10.5\text{ mm}$ . The following numerical simulation gives the results about the tube's crimping at  $8.5\text{ kV}$  voltage load. Figure 7  
230 represents the coil-tube setup and shows the crimping process of the tube.

Figure 8 gives the current density magnitude during this process. The current density distribution is referring to the generated eddy currents due to the magnetic field induced by the massive coil. These figures represent the tube's radial deformation at  $4\ \mu s$  (8.a),  $8\ \mu s$  (8.b),  $14\ \mu s$  (8.c) and  $22\ \mu s$  (8.d). The  
235 results obtained from these figures demonstrate that the current presents a high and an intense magnitude and is mainly concentrated at the center of the coil and the tube. This result is explained by the fact that the current always pursues the shortest path in the conductor. From figures 8-b and 8-c, the current

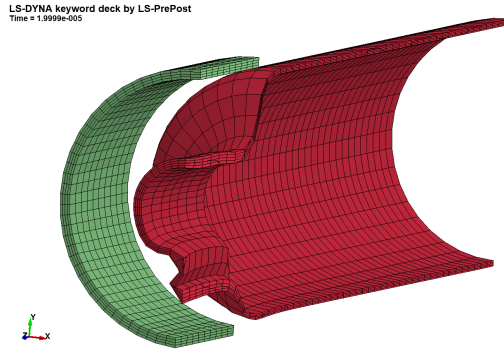


Figure 7: Representation of the tube's compression at  $20 \mu s$ .

density shows higher magnitudes in the outside periphery of the coil and the  
 240 tube which is due to the variation of the current pulse.

The Lorentz force distribution is plotted radially and axially in the pieces.  
 Figure 9 illustrates the distribution of the Lorentz force radially in the coil and  
 the tube. As shown in these figures, the Lorentz force is always increasing from  
 the inside to the outside surface of the tube. This is explained by the fact that  
 245 the magnetic field magnitude is decreasing from the inner radius of the coil to  
 its center. Figure 10 provides a general scheme of the process development, it  
 represents an axial deformation and Lorentz force distribution in the tube at  
 $4 \mu s$  (9.a),  $8 \mu s$  (9.b),  $14 \mu s$  (9.c) and  $22 \mu s$  (9.d). It presents the variation of  
 Lorentz force magnitude during the deformation process. What stands out in  
 250 both figures 8 and 10 is the concentration of both Lorentz force and current  
 density on the interior surfaces of the coil and the tube, that is to say in the  
 working zone.

A positive correlation is found between them by numerical analysis. Further-  
 more, an interesting result is the skin effect in the deformation area of the tube  
 255 and also on the interior surface of the coil. However, the deformation is almost  
 entirely uniform except in the gap between the input and the output bars. This  
 gap impacts the final deformation as it should be minimal in order to produce  
 a uniform magnetic field inside the coil and uniform shape of the tube. It is to  
 be noted that the initial gap between the coil and the tube changes the results

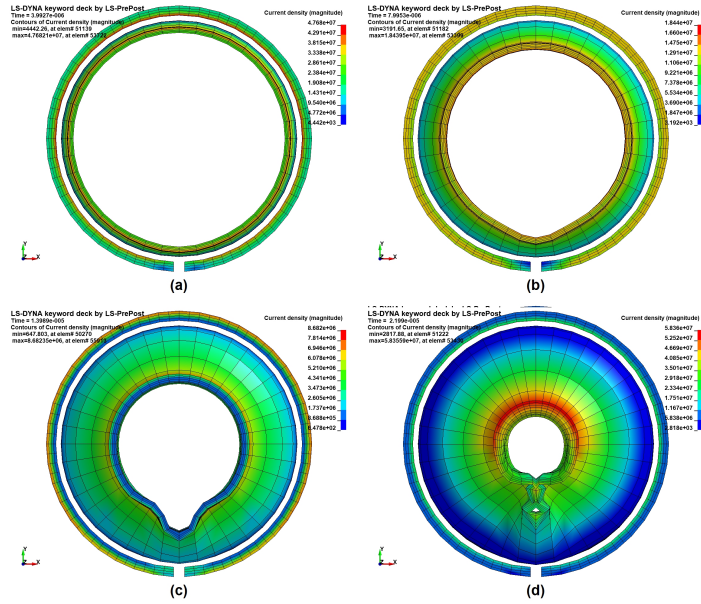


Figure 8: Current density magnitude distribution during deformation at: a)  $4 \mu s$ ; b)  $8 \mu s$ ; c)  $14 \mu s$ ; d)  $22 \mu s$ .

260 of the crimping process. The maximum values of Lorentz force and magnetic pressure are reached when this gap is initially set at the minimum possible.

To analyze the impact of the voltage load on the deformation of the tube, three figures are represented in figure 11 and illustrate the tube's deformation and the Lorentz force distribution for  $2.5 kV$ ,  $5.5 kV$  and  $8.5 kV$  voltage loads  
 265 at  $22 \mu s$ . These figures prove that the Lorentz force is increasing when the voltage is higher. This leads to produce higher pressure on the tube and as a result a strong crimping.

Afterwards, we can find radial Lorentz force, magnetic pressure as well as the velocity variations in one element of the tube. This element is located at  
 270 the front edge of the outer cylinder of the tube. The main characteristics and variables of the process are shown in figures 12 and 13 illustrating respectively, the development of Lorentz force magnitude and magnetic pressure over time at the center of the coil and in the tube-coil working zone.

Magnetic pressure, Lorentz force and velocity are obtained at the outer ra-

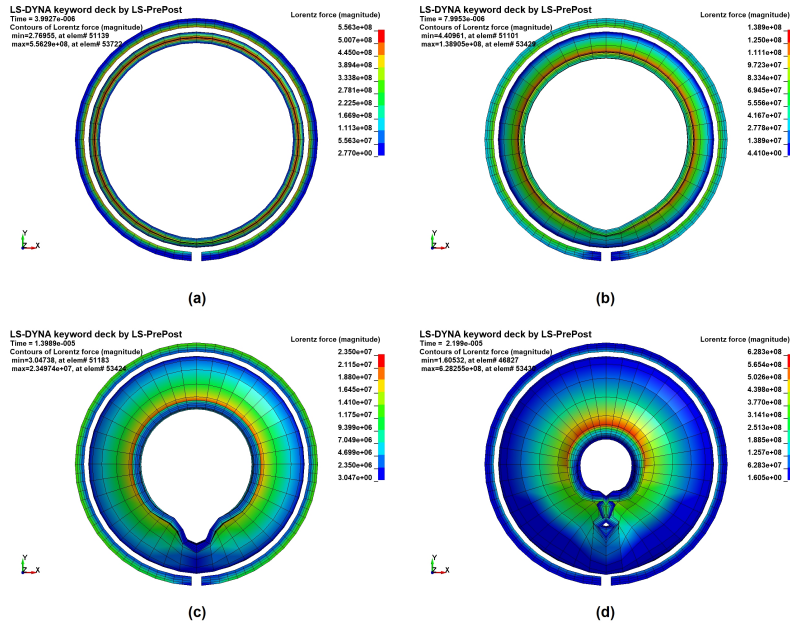


Figure 9: Representation of the Lorentz force distribution radially during deformation at: a) 4  $\mu\text{s}$ ; b) 8  $\mu\text{s}$ ; c) 14  $\mu\text{s}$ ; d) 22  $\mu\text{s}$ .

275 dius of the tube, exactly at the finite element with coordinates  $x, y, z = 0, 10.5, 0$ . At this point, both magnitudes are maximum for each voltage load, while we notice the minimum at  $x, y, z = 0, -10.5, 0$  corresponding to the gap of the input and output bars of the current. This result indicates that the Lorentz force increases if the gap between the coil and the tube decreases. Therefore,

280 in order to obtain the maximum deformation, the gap needs to be very small, which enables us to have the maximum magnetic impact on the work-piece. In the results illustrated in figures 12 and 13, we observe a time difference between the peaks in the graphs. A possible explanation for the magnetic pressure peak might be that it is based on the force variation in the element's thickness. The

285 pressure is produced due to the Lorentz force applied on the cross-section of the tube, and we cannot say that its peak should correspond exactly to the peak of this force at the same time. Another interesting finding was that the Lorentz force peak is not generated at the same time as the peak of the current

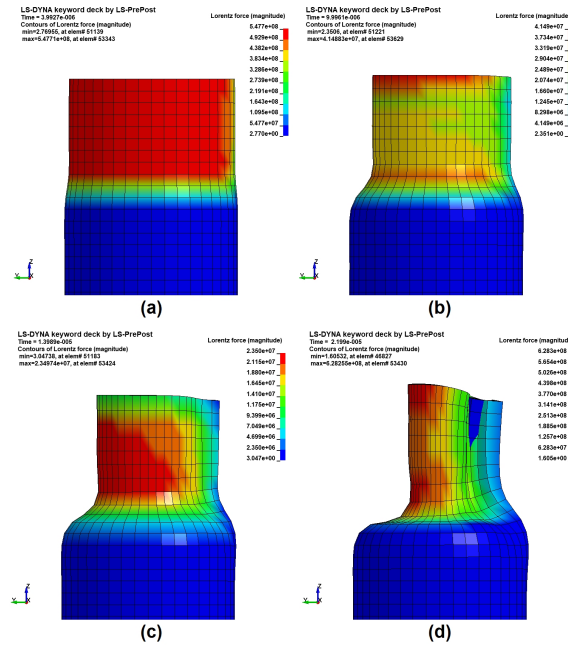


Figure 10: Lorentz force distribution in the outer surface of the tube at: a)  $4 \mu s$ ; b)  $8 \mu s$ ; c)  $14 \mu s$ ; d)  $22 \mu s$ .

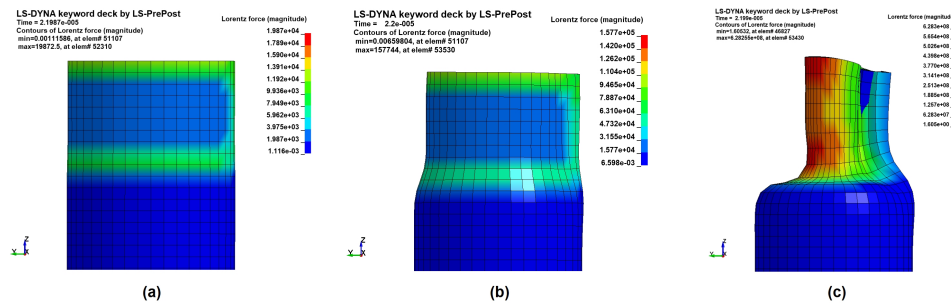


Figure 11: Lorentz force distribution for various voltage loads: a)  $2.5 kV$ ; b)  $5.5 kV$ ; c)  $8.5 kV$

290 pulse. This discrepancy could be attributed to the fact that the Lorentz force is produced due to the magnetic field  $B$  generated by the coil and the current density in the tube, this current density is based on the current  $I_t$  in the tube expressed by the previous Eq. (2). As mentioned in this formula,  $I_t$  expresses a

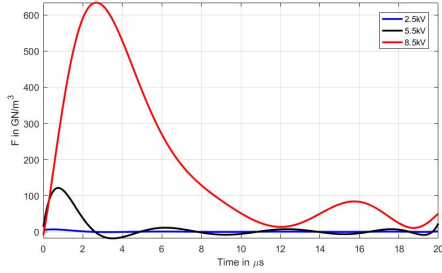


Figure 12: Variation of the Lorentz force density at 2.5 kV, 5.5 kV and 8.5 kV

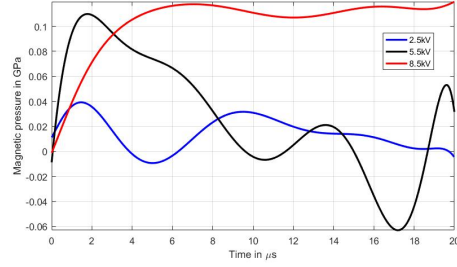


Figure 13: Variation of the magnetic pressure at 2.5 kV, 5.5 kV and 8.5 kV

phase shift of  $\pi/2$ , and therefore, the Lorentz force also presents a phase shift according to Eq. (22) which may explain the time difference between the current and the force plots.

In figure 14, we represent the velocity variation at various voltage loads. The results show that the deformation velocity is higher when we apply the maximum load.

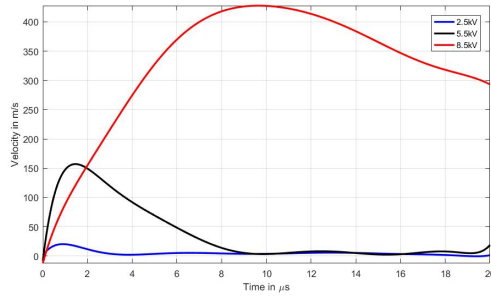


Figure 14: Variation of the velocity at 2.5 kV, 5.5 kV and 8.5 kV

At 8.5 kV, we reach a high velocity of 420 m/s while at 2.5 kV, we reach 25 m/s which explain the non deformation of the tube at this load. At 5.5 kV, we reach a velocity of 150 m/s. To validate the velocity data in this field, we compared our results to some existing experimental studies that are cited in the introduction section. In [19], the velocity measured using a Photon Doppler

Velocimetry (PDV) system reaches 160  $m/s$  at about 8  $kV$  and a current peak  
 of 300  $kA$ . This result corresponds to the one where the load is 5.5  $kV$ . The  
 305 difference between the two results may be due to the coil and the tube's geometry  
 but as well as the EMPG parameters. In the study conducted by [8], the velocity  
 reaches experimentally 300  $m/s$  with a current peak of 300  $kA$ . Furthermore,  
 the velocity reaches about 270  $m/s$  at about 380  $kA$  in [20]. All these results  
 310 show that this process produces a very high velocity to reach the deformation of  
 the work-piece. However and to the best of our knowledge, we did not find the  
 same coil geometry in previous studies and consequently, we cannot precisely  
 conclude the validation of our results using previous experimental researches.

## 5.2. Analytical results

315 This section aims to compare the two results (numerical and analytical) and  
 to examine the electrical parameters of the coil and the tube. It is worth nothing  
 that results provided in this section present only the magnitude of each parame-  
 ter and do not give their variations at any time during the crimping process. The  
 following results are given for radius  $R_1 = 11\text{ mm}$ ,  $R_2 = 11.5\text{ mm}$ ,  $R_3 = 10\text{ mm}$   
 320 and  $R_4 = 10.5\text{ mm}$ . For the geometry configuration as represented in figure  
 3, we begin by stating the self-inductance, resistance and mutual inductance of  
 the tube and the coil as stated in the table 4.

Table 4: Electrical parameters of the coil and the tube

$L(nH/m)$	$R(m\Omega)$	$L_t(nH/m)$	$R_t(m\Omega)$	$M_{ct}(nH/m)$
6.5	1.74	1.75	6.4	1.37

The results obtained from the table above gives an insight into the coupling  
 coefficient  $K = \frac{M_{ct}}{\sqrt{L.L_t}}$  of the system. In this case, it has a value of 0.4. This  
 325 result is very significant as it specifies how the magnetic flux produced by the  
 coil will interact with the tube.

The second set of results focuses on the analytical method where the load

voltage is  $8.5 \text{ kV}$ . For this value, the current magnitudes  $I_c$  and  $I_t$  in both the coil and the tube are given respectively by  $I_c = 2.43e3 \text{ kA}$  and  $I_t = 1.009 \text{ kA}$ .

330 Using Eq. (26)  $\vec{B} = \mu\vec{H}$ , the magnetic field magnitude  $B$ , which is generated in the outer radius of the tube at the deformation area, has a value of  $B = 63.76 \text{ T}$ , while at the inner radius of the tube, it is about  $B = 69 \text{ T}$ . It is apparent from this data that the magnetic field generated in the coil-tube gap is very intense. These parameters are decreasing when the voltage load is decreasing.

335 If we now turn to Lorentz force and magnetic pressure acting directly on the tube, we find remarkable results; as follows: the Lorentz force magnitude at the outer radius of the tube is about  $F = 625 \text{ GN}$  while the magnetic pressure is about  $P = 0.16 \text{ GPa}$ . At  $8.5 \text{ kV}$ , both magnitudes increase from the outer radius to the inner radius of the tube. Consequently, we find that at the inner

340 radius, Lorentz force is about  $639 \text{ GN}$  while the magnetic pressure is about  $0.193 \text{ GPa}$ . However, at  $2.5 \text{ kV}$  and  $5.5 \text{ kV}$ , we found that these parameters are decreasing from the inner radius to the outer radius of the tube. These results may be explained by the fact that the magnetic field reaches maximum values at the inner radius of the tube. As for the numerical simulation results,

345 the Lorentz force at the outer radius is about  $654 \text{ GN}$  while the magnetic pressure is  $0.17 \text{ GPa}$  which corresponds to the analytic results. The last part of the results is illustrated in figures 15 and 16. It provides a comparison of the Lorentz force (figure 15) and the magnetic pressure (figure 16) analytically and by numerical simulation at the outer radius of the tube.

350 From these figures, we conclude that the analytic results are almost similar to the numerical ones at  $2.5 \text{ kV}$  and  $8.5 \text{ kV}$ . However at  $5.5 \text{ kV}$ , according to the numerical results, we observe a significant error of 15% precisely in the magnetic pressure. As a conclusion, these results suggest that there is an association between the analytic model and the numerical one. They also provide important

355 insights into the modeling of the process based on the electrical parameters of the coil and the work-piece.

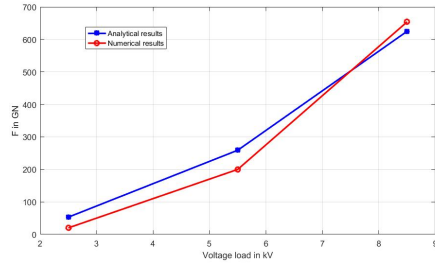


Figure 15: Comparison of the Lorentz force at 2.5 kV, 5.5 kV and 8.5 kV

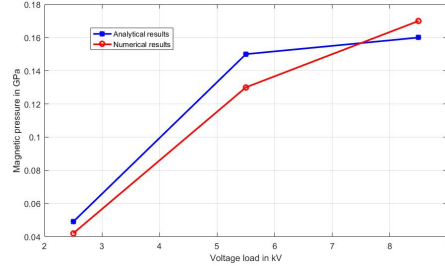


Figure 16: Comparison of the magnetic pressure at 2.5 kV, 5.5 kV and 8.5 kV

## 6. Conclusion and perspectives

The main objective of this study is to identify Lorentz force and the magnetic pressure analytically and by numerical simulations in the case of crimping a metallic tube using an electromagnetic pulse generator. The most prominent finding to emerge from this study is that both methods give a maximum value of the force when the voltage load is higher. The first contribution is to determine the analytical Lorentz force applied to a metallic tube. The analytic method has identified the self-inductance and the resistances of the coil and the tube as well as the mutual inductance. The second contribution of this work was dedicated to the numerical method based on Maxwell equations, where the results of the deformation pattern are estimated numerically. The findings reflect those of a similar study of the tube crimping process by a multi-turn solenoid coil [18]. The maximum magnetic pressure  $P_{max}$  found at 8.5 kV is  $P_{max} = 0.17 \text{ GPa}$ . This value provides a higher deformation of the tube. In the current research work, the numerical and analytical findings give almost the same Lorentz force magnitude at the coil-tube working zone as well as the magnetic pressure except at 5.5 kV load where we observed a significant error in the magnetic pressure results. These results provide a strong hypothesis that our model presents the parameters of the coil and the work-piece properly. A comparison of the two results shows that both methods give the same results of both magnitudes.

Overall, these results provide valuable insights into the representation of the crimping process analytically since the amount of time for analytical calculations does not exceed 3 seconds. However, the numerical method is very demanding  
380 in terms of computing time (about 3 hours). The main weakness of this study is that the analytical model does not consider the variation through time of the magnetic parameters in both the tube and the coil, which could be usefully explored in future research work. Furthermore, instead of the crimping process, an additional study could assess the electromagnetic pulse welding process using  
385 the developed methods in this paper.

### Acknowledgment

Authors would like to gratefully thank Hauts-de-France region for its financial support and for the Innovaltech platform that served as the experimental platform for our research work.

### 390 References

- [1] K. Sofi, M. Hamzaoui, H. Elidrissi, A. Nait Sidi Moh, A. Hamzaoui, Experimental study of magnetic pulse generator and the field shaper effect on the current pulse, in: 2018 Renewable Energies, Power Systems & Green Inclusive Economy (REPS-GIE), 2018, pp. 1–5. doi:10.1109/REPSGIE.2018.8488862.  
395
- [2] TWI Ltd for the Health and Safety Executive, Measurement and Analysis of Magnetic Fields from Welding Processes, Tech. rep. (2005).  
URL <https://www.hse.gov.uk/research/rrpdf/rr338.pdf> (Lastvisit:12/2019)
- [3] K. Sofi, M. Hamzaoui, H. E. Idrissi, A. Nait Sidi Moh, A. Hamzaoui, Analysis of electromagnetic field generated by a magnetic pulse joining machine, in: 8th International Conference on High Speed Forming, Vol. ICHSF2018, 2018.  
400

URL [https://eldorado.tu-dortmund.de/bitstream/2003/36953/1/](https://eldorado.tu-dortmund.de/bitstream/2003/36953/1/ICHSF2018-Paper_{_}SOFI.pdf)  
405 ICHSF2018-Paper\_{\_}SOFI.pdf

- [4] K. Sofi, H. El Idrissi, M. Hamzaoui, A. Hamzaoui, L. C. Alaoui, F. Bougrioua, D. Jouaffre, M. Morel, D. Haye, Current and temperature distribution in a massive one turn coil used in electromagnetic pulse generator, in: 2017 18th International Symposium on Electromagnetic Fields in Mechatronics, Electrical and Electronic Engineering, ISEF 2017, IEEE, 2017, pp. 1–2. doi:10.1109/ISEF.2017.8090724.
- [5] O. Mansouri, O. Maloberti, Analytical 1D-calculation of a 1-turn Coil Parameters for the Magneto-Forming Technology Analytical 1D-calculation of a 1-turn Coil Parameters for the Magneto-Forming Technology, in: 7th 415 International Conference on High Speed Forming 2016 82, no. April, 2016. doi:10.17877/DE290R-16975.
- [6] J. Cui, G. Sun, G. Li, Z. Xu, P. K. Chu, Specific wave interface and its formation during magnetic pulse welding, Applied Physics Letters 105 (22) (2014) 1–5. doi:10.1063/1.4903044.
- [7] J. Cui, G. Sun, J. Xu, Z. Xu, X. Huang, G. Li, A study on the critical 420 wall thickness of the inner tube for magnetic pulse welding of tubular Al-Fe parts, Journal of Materials Processing Technology 227 (2016) 138–146. doi:10.1016/j.jmatprotec.2015.08.008.
- [8] J. Cui, Y. Li, Q. Liu, X. Zhang, Z. Xu, G. Li, Joining of tubular carbon 425 fiber-reinforced plastic/aluminum by magnetic pulse welding, Journal of Materials Processing Technology 264 (September 2018) (2019) 273–282. doi:10.1016/j.jmatprotec.2018.09.018.
- [9] C. Weddeling, V. Walter, P. Haupt, A. E. Tekkaya, V. Schulze, K. A. Weidenmann, Joining zone design for electromagnetically crimped connections, Journal of Materials Processing Technology 225 (2015) 240–261. 430 doi:10.1016/j.jmatprotec.2015.06.009.

- [10] C. Weddeling, O. K. Demir, P. Haupt, A. E. Tekkaya, Analytical methodology for the process design of electromagnetic crimping, *Journal of Materials Processing Technology* 222 (2015) 163–180. doi:10.1016/j.jmatprotec.2015.02.042.
- 435
- [11] A. K. Rajak, S. D. Kore, Experimental investigation of aluminium-copper wire crimping with electromagnetic process: Its advantages over conventional process, *Journal of Manufacturing Processes* 26 (2017) 57–66. doi:10.1016/j.jmapro.2017.01.009.
- 440 [12] A. K. Rajak, S. D. Kore, Comparison of different types of coil in Electromagnetic terminal - wire crimping process: Numerical and experimental analysis, *Journal of Manufacturing Processes* 34 (February) (2018) 329–338. doi:10.1016/j.jmapro.2018.06.025.
- 445 [13] A. K. Rajak, S. D. Kore, Numerical simulation and experimental study on electromagnetic crimping of aluminium terminal to copper wire strands, *Electric Power Systems Research* 163 (2018) 744–753. doi:10.1016/j.epsr.2017.08.014.
- [14] H. Cramer, M. Mueller, L. Appel, Enhanced joint properties by magnetic pulse crimping with filler material, *Advanced Materials Research* 1029 (2014) 37–43. doi:10.4028/www.scientific.net/AMR.1029.37.
- 450 [15] K. Shanthala, T. N. Sreenivasa, H. Choudhury, S. Dond, A. Sharma, Analytical, numerical and experimental study on joining of aluminium tube to dissimilar steel rods by electro magnetic pulse force, *Journal of Mechanical Science and Technology* 32 (4) (2018) 1725–1732. doi:10.1007/s12206-018-0328-0.
- 455 [16] K. Shanthala, T. N. Sreenivasa, H. N. Murthy, S. Dond, H. Choudhury, A. Sharma, Joining of tubular steel-steel by unconventional magnetic pulse force: environmentally friendly technology, *Bulletin of Materials Science* 42 (6). doi:10.1007/s12034-019-1947-5.

- 460 [17] Z. Lai, Q. Cao, B. Zhang, X. Han, Z. Zhou, Q. Xiong, X. Zhang, Q. Chen, L. Li, Radial Lorentz force augmented deep drawing for large drawing ratio using a novel dual-coil electromagnetic forming system, *Journal of Materials Processing Technology* 222 (2015) 13–20. doi:10.1016/j.jmatprotec.2015.02.029.
- 465 [18] G. Areda, S. Kore, Finite Element Modeling and Simulation of Electromagnetic Crimping of Al6016-T6 Tube with Steel Rod, *Proceedings of the International Conference on Communication and Signal Processing 2016* 137 (1) (2016) 83–88.
- [19] A. Nassiri, C. Campbell, G. Chini, B. Kinsey, Analytical Model and Experimental Validation of Single Turn, Axi-symmetric Coil for Electromagnetic Forming and Welding, *Procedia Manufacturing* 1 (2015) 814–827. doi:10.1016/j.promfg.2015.09.070.
- 470 [20] B. Kinsey, A. Nassiri, Analytical model and experimental investigation of electromagnetic tube compression with axi-symmetric coil and field shaper, *CIRP Annals - Manufacturing Technology* 66 (1) (2017) 273–276. doi:10.1016/j.cirp.2017.04.121.
- 475 [21] C. Akyel, S. I. Babic, K. E. Wu, J. F. Mojica, Mutual Inductance of Thin Coaxial Circular Coils with Constant Current Density in Air ( Filament Method ), *Proceedings of the WSEAS International Conferences, Istanbul, Turkey, May 27-29, 2006* (2006) 168–175.
- 480 [22] E. B. Rosa, F. W. Grover, Formulas and Tables for the Calculation of Mutual and Self-Inductance, *Bulletin of the Bureau of Standards* 8 (1912) 1–287. doi:10.6028/bulletin.185.
- [23] J. T. Conway, Inductance calculations for noncoaxial coils using bessel functions, *IEEE Transactions on Magnetics* 43 (3) (2007) 1023–1034. doi:10.1109/TMAG.2006.888565.
- 485

- [24] R. Ravaut, G. Lemarquand, V. Lemarquand, S. I. Babic, C. Akyel, Mutual Inductance And Force Exerted Between Thick Coils, Progress In Electromagnetics Research 102 (2010) 367–380. doi:10.2528/PIER10012806.
- 490 [25] A. Hamzaoui, Conception et réalisation d'un système de transfert d'énergie et d'informations sans contact : Application à la télé-alimentation d'un système à deux axes (jan 2008).  
URL <https://www.theses.fr/2008AMIE0117><https://www.theses.fr/138444609>
- 495 [26] J. Hallquist, LS-DYNA® theory manual, no. March, 2006.  
URL [http://www.dynasupport.com/manuals/additional/ls-dyna-theory-manual-2005-beta/at{}\\_download/file](http://www.dynasupport.com/manuals/additional/ls-dyna-theory-manual-2005-beta/at{}_download/file)
- [27] LSTC, LS-DYNA Keyword User's Manual - Volume III - Multi-Physics Solvers, Vol. III, 2017.  
500 URL <http://www.dynasupport.com/manuals/ls-dyna-manuals/ls-dyna-manual-r10.0-vol-iii>
- [28] T. Župan, Ž. Štih, B. Trkulja, Fast and Precise Method for Inductance Calculation of Coaxial Circular Coils with Rectangular Cross Section Using the One-Dimensional Integration of Elementary Functions Applicable to Superconducting Magnets, IEEE Transactions on Applied Superconductivity 24 (2) (2014) 81–89. doi:10.1109/TASC.2014.2301765.  
505
- [29] Z. Piatek, B. Baron, Exact Closed Form Formula for Self Inductance of Conductor of Rectangular Cross Section, Progress In Electromagnetics Research M 26 (January 2012) (2014) 225–236. doi:10.2528/pierm12080314.  
510
- [30] Y. U. Haiping, L. I. Chunfeng, Effects of current frequency on electromagnetic tube compression, Journal of Materials Processing Technology 209 (2) (2009) 1053–1059. doi:10.1016/j.jmatprotec.2008.03.011.

515 [31] R. Ravaut, G. Lemarquand, V. Lemarquand, S. Babic, C. Akyel, Calculation of the magnetic field created by a thick coil, *Journal of Electromagnetic Waves and Applications* 24 (10) (2010) 1405–1418. doi: 10.1163/156939310791958653.

[32] Online Materials Information Resource - MatWeb.  
URL <http://www.matweb.com/>